Journal of Applied Fluid Mechanics, Vol. 16, No. 7, pp. 1316-1330, 2023.
Available online at www.jafmonline.net, ISSN 1735-3572, EISSN 1735-3645.
https://doi.org/10.47176/jafm.16.07.1634

Coupling Bionic Design and Numerical Simulation of the Wavy Leading-Edge and Seagull Airfoil of Axial Flow Blade for Air-conditioner

J. Tan[1, 2], P. Dong[2†], J. Gao[1, 2], C. Wang[1, 2] and L. Zhang[1, 2]

[1]*School of Mechanical Engineering, Yancheng Institute of Technology, Yancheng 224051, P.R. China*
[2]*Key Laboratory for Advanced Technology in Environmental Protection of Jiangsu Province, Yancheng Institute of Technology, Yancheng 224051, P. R. China*

[†]*Corresponding Author Emails: dongpy11@ycit.edu.cn*

(Received October 22, 2022; accepted March 1, 2023)

ABSTRACT

It is essential to maintain the aerodynamic performance of the air-conditioning system meanwhile reducing the noises (including aerodynamic, broadband, and discrete noises), determining the consumer's comfort level. In this work, depending on the coupling of the wavy leading-edge and the seagull airfoil, the aeroacoustics noise and aerodynamic performance of the impellers with the coupling bionic blade were investigated in detail. The results indicate the aerodynamic performance was improved by the coupling bionic optimization. Moreover, the total pressure efficiency (η) of the coupling bionic blade increases by 2.28% in comparison to the original blade. Furthermore, A smaller static differential pressure is observed between the suction and pressure sides, and vortices and backflows from the pressure side to the suction side are hampered, causing a reduction in turbulence noise. Additionally, the broadband noise of the coupling bionic blade decreases by 3.59 dB. Besides, the coupling bionic blade improves the directivity of the sound pressure level, especially in the middle-frequency and low-frequency region, resulting in a decrease of 7.9 dB for the aeroacoustics noise of the coupling bionic blade. What's more, the modal analysis demonstrates the security of the designed coupling bionic blade. In generally, this work provides some inspiration to design axial flow fans with excellent aerodynamic performance and low-noise characteristics.

Keywords: Aerodynamic performance; Bionic coupling design; Noise reduction; Wavy leading-edge; Axial flow fan.

NOMENCLATURE

Ac	air-conditioner	Le	leading-edge
Aff	axial flow fan	Lf	low-frequency
Bt	blade tip	Mf	middle-frequency
CFD	Computational Fluid Dynamics	Ps	pressure side
EXP	experiment	RANS	Reynolds-Averaged Navier-Stokes
FFT	Fast Fourier Transformation	SPL	Sound Pressure Level
FW-H	Ffowcs Williams and Hawkings	Ss	suction side
LES	Large-Eddy Simulations	Te	trailing-edge

1. Introduction

With the rapid economic and social development, there is a growing requirement for a comfortable living environment. Accordingly, there is a persistent increase in demand for household appliances that control indoor air such as an Ac. The Ac is always performed continuously, resulting in excessive and tiring noise to the consumers. Consequently, relevant developers are constantly investing in research to lessen the aeroacoustics noise and enhance the aerodynamic performance of Acs.

As the fundamental component of the Acs, the Aff contributes the primary noise during operation. Hence, it is essential to maintain the aerodynamic performance while reducing the noise, determining the consumer's satisfaction (Lim *et al.* 2020). Turbulent vortexes generated by unreasonable flow inside are considered the essential contributing factor to fan noise according to the vortex-sound theory. Hence, it is significant to avoid turbulent

vortexes when designing the Aff. Moreover, optimizing fan noise can indirectly reduce energy consumption (Schram and Hirschberg 2003). Therefore, it is highly desired to design novel Affs with excellent aerodynamic performance, and low noise (Jung and Joo 2019). As the key power component of the Aff, it is essential to investigate the blade through rational design to lessen the aeroacoustics noise and enhance the aerodynamic performance of Acs.

In recent years, the Le and Te of the blade were reasonably constructed, which can expand the wake region and accelerate the break of vortices (Choi 1994; Liu H 2003; Xu *et al.* 2015). The optimized Le can dramatically lower the flow loss compared with the optimized Te (Liu *et al.* 2021a). Considerable research efforts have been devoted to improving Aff performance by modifying the Le shape. And the results demonstrated the serration Le is an extremely effective strategy for reducing airfoil noise, in particular for the high turbulence intensity at the airfoil's Tu upstream under distorted flow conditions (Kim *et al.* 2016; Chaitanya *et al.* 2017). The Aff with sinusoidal serrations Le exhibited a reduction in the SPL (Corsini *et al.* 2014; Biedermann *et al.* 2019). In addition, various serrations Le (single-sine, double-sine, and random-amplitude serrations) were designed and investigated, and the results indicate the sinusoidal serration Le demonstrated the best noise-reduction characteristics (Krömer *et al.* 2018b; Kroemer *et al.* 2019). A more generic Le serration with different amplitudes and wavelengths was investigated, illustrating that the optimized Le could lessen the aerodynamic and broadband noise both (Kroemer *et al.* 2018; Tong *et al.* 2018; Bian *et al.* 2019; Kroemer *et al.* 2018a; Tong *et al.* 2021). Furthermore, the biological structure screened by nature was utilized in the design of the Le with the bionic mechanism analysis, such as the owls' comb-like Le and the humpback whale flippers' tubercles Le, demonstrating the biological structure can inhibit the separation of the boundary layer, resulting in excellent aerodynamic performance and noise reduction (Yan *et al.* 2020; Chen *et al.* 2021b; Dong and Dou 2021; Liu *et al.* 2021b; Wu and Liu 2021; Zhang *et al.* 2021). However, the reported bionic Le mostly displayed serration, which is difficult to be manufactured and will be likely to be worn during long-term operations.

Additionally, it is necessary to design an airfoil of the blade with low-noise characteristics and excellent aerodynamic performance. In recent years, the optimization of the airfoil has been intensively investigated (Abdolmaleki *et al.* 2019; Balla and Vad 2019; Wu and Huang 2019; Takahashi *et al.* 2020). Especially, various bionic airfoils were widely used, such as the cross-section of owl wing (Wang and Liu 2019; Li *et al.* 2020; Chen *et al.* 2021; Gao *et al.* 2021; Li *et al.* 2021; Wang *et al.* 2021; Li *et al.* 2022; Wang *et al.* 2022) possessed the excellent noise reduction characteristic and the streamlined geometric features of sturgeons (Yan *et al.* 2019, 2020) exhibited a high lift-drag ratio. Besides, seagull wings displayed low-noise characteristics and excellent aerodynamic performance (Chang *et al.* 2019; Hua *et al.* 2019; Wu *et al.* 2022).

As we all know, there is little research on the coupling of bionic wavy Le and airfoil of the blade with complex structures. In this study, we designed a bionic coupling blade for the Aff, determined by the cross-section of the seagull wing and the wavy Le, combining seagull wing configuration characteristics and the characteristics of the wave, which has the capability for noise reduction and wear resistance. Depending on the coupling of the wavy Le and the seagull airfoil, the aeroacoustics noise and aerodynamic performance of the impellers with the coupling bionic blade were investigated in detail.

2. NUMERICAL METHODS

2.1 Calculation model

Four impellers were constructed to analyze the characteristics of bionics blades for the Aff. Figure 1 presents the unique shape of impellers with various bionic structures. I-1 denotes the original blade; I-2 denotes the wavy Le blade; I-3 denotes the bionic airfoil blade; I-4 denotes the coupling bionic blade with the wavy Le and the bionic airfoil. Among them, the amplitude (A) of the wave was set to 5 mm and the wavelength (W) of that was set to 20.60 mm.

Besides, the 40% cross-section of seagull wings was applied as the bionic airfoil. On the basis of the study of Hua on seagull (Hua 2013), the baseline airfoil was reconstructed. The thickness distribution of the wing and the camber line were obtained by least-squares fitting. The upper and lower surface of airfoil profiles could be parameterized through adding and subtracting operations concerning the camber line according to the following Eq. (1–2) (Wang *et al.* 2022).

$$Z_{up} = Z_{(c)} + Z_{(t)} \tag{1}$$

$$Z_{low} = Z_{(c)} - Z_{(t)} \tag{2}$$

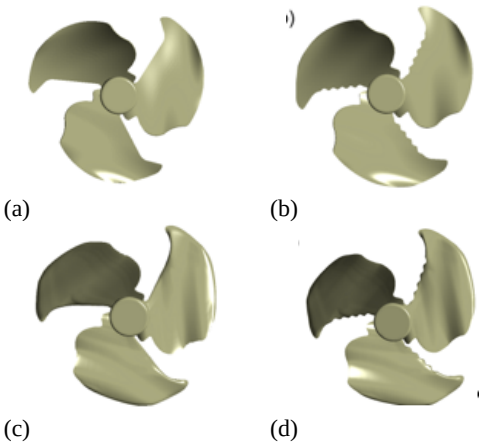

Fig. 1. Designed structures:(a) I-1, (b) I-2, (c) I-3, and (d) I-4.

Table 1 Coefficients referring to seagull wing.

	$n = 1$	$n = 2$	$n = 3$	$n = 4$
S_n	3.876	–0.806	0.771	–
A_n	–15.245	26.481	–18.976	4.623

where Z_{up} represents the upper surface molded line, Z_{low} denotes the lower surface molded line, $Z_{(c)}$ and $Z_{(t)}$ represents the coordinate of camber line and thickness, respectively.

The distribution of the coordinate of the camber line ($Z_{(c)}$) and the coordinate of a thickness ($Z_{(t)}$) could be calculated by Eqs. (3–4) (Wang *et al.* 2022).

$$\frac{Z_{(c)}}{c} = \frac{Z_{(c)\max}}{c}\eta(1-\eta)\sum_{n=1}^{3} S_n (2\eta - 1)^{n-1} \tag{3}$$

$$\frac{Z_{(t)}}{c} = \frac{Z_{(t)\max}}{c}\sum_{n=1}^{4} A_n \left(\eta^{n+1} - \sqrt{\eta}\right) \tag{4}$$

where $Z_{(c)max}$ and $Z_{(t)max}$ represent the maximum values of the coordinate of the camber line and the coordinate of thickness, respectively. The coefficients of A_n and S_n were used to describe the seagull, which were summarized in Table 1. $\eta = n/c$ represents the normalized coordinate of chordwise and c denotes the chord length.

The $Z_{(c)max}$ and $Z_{(t)max}$ were calculated by Eqs. (5–6) (Wang *et al.* 2022).

$$Z_{(c)\max}/c = 0.14/\left(1 + 1.32\xi^{1.4}\right) \tag{5}$$

$$Z_{(t)\max}/c = 0.1/\left(1 + 3.545\xi^{1.4}\right) \tag{6}$$

where ξ (0.4) represents the coordinate of relative position along the spanwise direction. Hence, the airfoil of the seagull wing on 40% cross-section was extracted (Hua 2013), which has the characteristics of superior aeroacoustics performance. Figure 2 depicts the distribution of the designed bionic seagull airfoil.

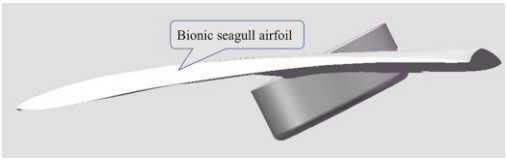

Fig. 2. Designed bionic seagull airfoil profile.

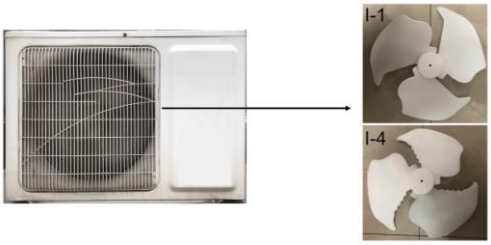

(a) (b)

Fig. 3. (a) Photograph of the Ac outdoor unit, and (b) impellers.

To provide an accurate flow in the impeller, the shield, the heat exchanger, the motor, and the bracket were omitted, and the compressor part was removed that does not affect the fan duct during modeling. Without regard to the influence of the grille, the simplified structure was created. Figure 3 illustrates the photograph of the Ac outdoor unit and impellers, which work at the speed of 850 rpm.

2.2 Grid Independent Analysis and Computational Domain

After being designed in SOLIDWORKS 2020, the computational domain grids were generated in ANSYS Fluent Meshing. As shown in Fig. 4, the domains were meshed by Ploy-Hexahedron core grids with less grids and the high precision of simulation. When applying the Realizable k-epsilon turbulence model, y^+ was set to be less than 1.

As the number of grids increases, the error resulting from the grids will decrease progressively. As illustrated in Fig. 5, grid independent analysis was performed by solving the flow rate (Q) and the broadband noise of 5 groups of grids with various. numbers ranging from 0.86 to 4.39 million. The

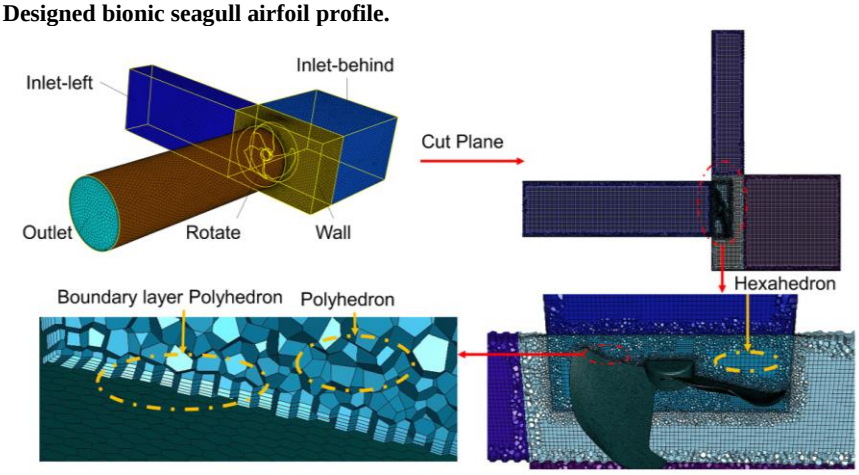

Fig. 4. Computational domain and grids.

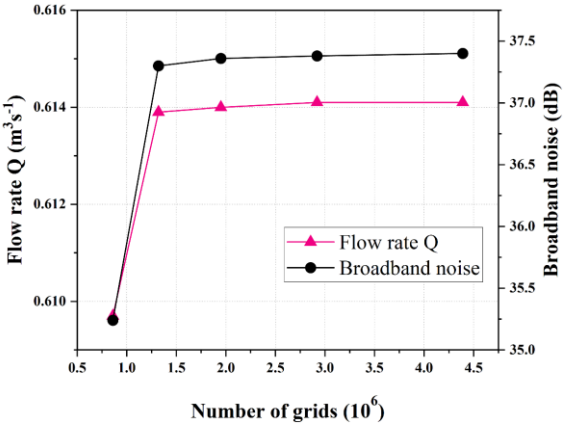

Fig. 5. Grid independence analysis for flow rate and broadband noise.

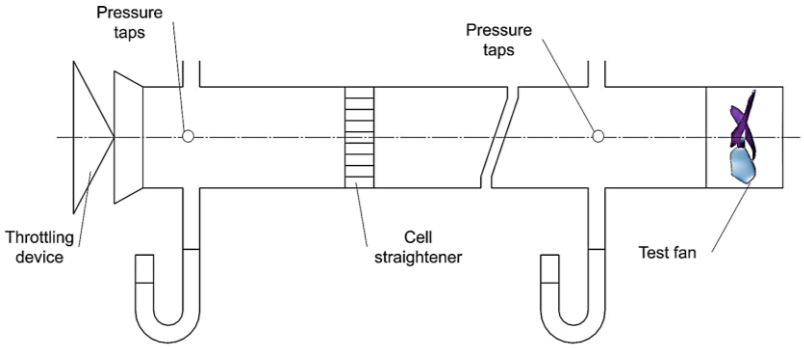

Fig. 6. Device diagram of aerodynamic performance test.

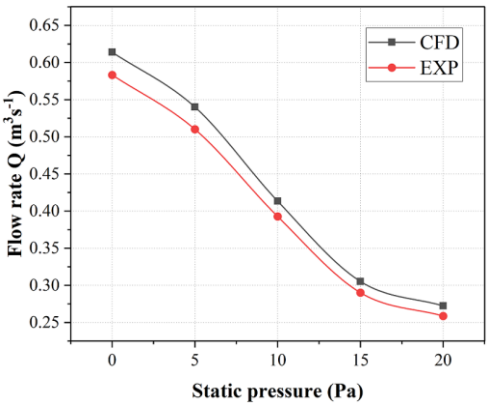

Fig. 7. A comparison of flow rate between CFD prediction and EXP data.

variations of broadband noise and Q were compared with 5 different grids numbers. The broadband noise and Q ascend with the growth of the grids number, while it will remain constant when the grids number exceeds 2.82 million. Therefore, the grids number of 2.82 million was eventually selected considering calculation time and precision.

2.3 Experimental Setup and a Comparison Between CFD Prediction and EXP Data

According to GB/T 1236-2017 (GB/T 2017), the aerodynamic performance was tested with the standard air duct. As depicted in Fig. 6, the test bench for aerodynamic measurements was illustrated with the schematic diagram, including throttling device, pressure taps, cell straightener and test fan, with testing accuracy at ± 1%.

Figure 7 displays the characteristic curve of the designed axial fan (I-4) from the CFD prediction and EXP results at the designed speed (n = 850 rpm). It is found that the numerical predictions of Q are higher than the EXP results in the whole range of sustained operation process, while the deviation of the CFD and EXP results is less than 5%, which is allowable by the relevant research (Sasaki *et al.* 2013; Wen *et al.* 2013). As we all know, there are two factors account for this deviation. The first factor is the geometry simplification: the shield, the heat exchanger, the motor, and the bracket were neglected during the CFD simulation, leading to be

easier for airflow to pass through. The other factor may be the unavoidable errors between the EXP test and CFD simulation. Therefore, it is accurate for the Aff to predict aerodynamic performance by the CFD simulation.

2.4 Turbulence Model

FLUENT was applied to numerically calculate the axial fan performance and its internal flow field to resolve the incompressible equations for RANS. In this work, the turbulence calculation model was the Realizable k-epsilon model, which is more realistic in the calculation of separation flow, boundary layer calculation, and cyclonic flow calculation. The coupling of pressure-velocity was the SIMPLE algorithm. The equations of energy, momentum, and turbulent dissipation were the second-order windward format. These models were available in the turbulent viscosity precisely calculation, and it was valid during solving eddies for noise prediction in the relevant research (Jiang *et al.* 2019). The pressure discretization was the PRESTO! format. The convergence indexes for the mass, velocity components, turbulent kinetic energy, and their dissipation terms were set to 10^{-6}.

In the aerodynamic noise analysis, the RANS simulation result was applied as the initiation of the acoustic field, and the Realizable k-epsilon model was replaced by the LES to obtain unsteady flow field parameters such as pressure pulsations on the surface of the sound source and then combined with FW-H, utilized for achieving the sound field in the source region (Lallier-Daniels *et al.* 2017). Subsequently, the sound field information such as the SPL and the time-averaged sound pressure pulsation in the source area was achieved. Compare with the wavelength of acoustic wave, the feature size of the fan can be ignored, hence the scattering, reflection, and diffraction noise were not taken into account in the noise calculation.

The time step was calculated according to the following Eq. (7) (Zuo *et al.* 2019).

$$\Delta t = 1/2\,f \tag{7}$$

where $\triangle t$ denotes the time step, and f represents the highest frequency that can be captured by the Fourier transformation. To save computational resources and costs meanwhile taking into account the computational efficiency and other issues, the research frequency band was set to 0–20 kHz because of the small contribution of the frequency band after 20 kHz to the overall SPL, and the computational time step was operated at 2.5×10^{-5} s.

2.5 Boundary Conditions

All boundary conditions were set to the wall with no-slip boundary conditions using the impeller region as the rotating region, and the speed was set to 850 rpm. The total pressure of inlet and the static pressure of outlet were set to 101325 Pa.

1. The impeller was in the rotational area rotating counterclockwise along the Z-axis; the rotating speed was given according to the actual speed of the motor at different operating points; the other areas were set as the stationary area; the MRF reference for the dynamic-static intersection in the RANS calculation, while the MRF method was replaced by the method of sliding mesh in the LES calculation.
2. Relative coordinate system was adopted for the blade wall surface relative to the impeller rotation area stationary, and the absolute stationary surface was utilized for the other wall surface of the fan.

2.6 Acoustic Modeling

The FW-H model was applied to predict the acoustic field based on the result of the flow field. FW-H extended the Light-hill's acoustic analogy taking into account the displacement of a rigid surface in the flow, which can be expressed as the following Eq. (8).

$$\left(\frac{\partial^2}{c_0^2}-\nabla^2\right)p'(x,t)=\frac{\partial}{\partial t}\left\{\left[\rho_0 v_n+\rho(u_n-v_v)\right]\delta(f)\right\}$$
$$-\frac{\partial}{\partial x_i}\left\{\left[\Delta p_{ij}n_j+\rho u_i(u_n-v_v)\right]\delta(f)\right\}+\frac{\partial^{-2}}{\partial x_i\partial x_j}\left[T_{ij}H(f)\right] \tag{8}$$

Where p denotes the static pressure of sources, p' represents acoustic pressure of the observer, c_0, ρ, u_i, n_j, and u_n denote the sound velocity, the density of air, the flow velocity, the surface normal vector and the normal surface velocity, respectively. Further, $\delta(f)$ represents the Dirac-delta, $H(f)$ denotes Heaviside functions, T_{ij} represents the Lighthill's stress tensor for acoustic field, which can be calculated by the following Eq. (9).

$$T_{ij}=\rho u_i u_j+p_{ij}-c_0^2\rho\delta_{ij} \tag{9}$$

Where $\rho u_i u_j$ denotes the monopole, p_{ij} represents the dipole, and $c_0^2\rho\delta_{ij}$ denotes the quadrupole sources. In the case of fan noise, the dipole sources are primary (Neise 1992). What's more, the dipole term was applied to forecast the pressure pulsation on the blades surface (Brentner 1988; Farassat and Brentner 1998).

Consequently, the dipole term was applied to forecast the acoustic field produced by the blades in this study. Lowson's formula can be applied to calculate the dipole source term, and it can be calculated by the following Eq. (10).

$$4\pi r p'(x,t)=\sum\left[\begin{array}{l}\dfrac{1}{c_0(1-M_r)^2}\left(F_r+\dfrac{F_r M_r}{(1-M_r)}\right)\\ +\dfrac{1}{r(1-M_r)^2}\left(F_r\dfrac{(1-M^2)}{(1-M_r)}+F_i M_i\right)\end{array}\right]_{ret} \tag{10}$$

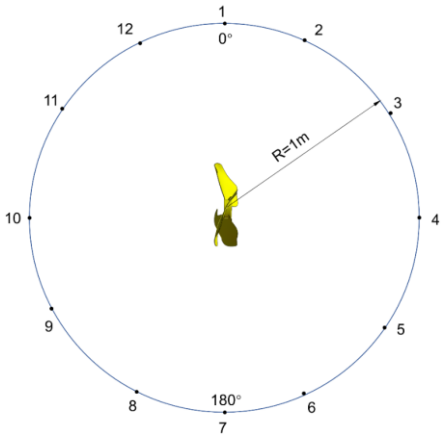

Fig. 8. Distribution of monitoring points.

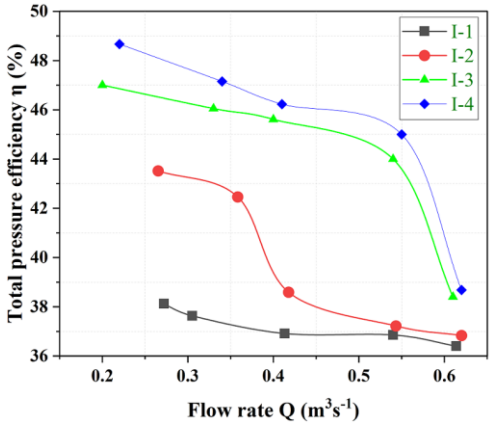

Fig. 9. Total pressure efficiency.

Where, x_i denotes the position of the observer, y_i represents the position of the source, r denotes the distance of x_i and y_i. In addition, F_i denotes the force of the source, F_r denotes the force of the source in the direction of radiation, M_i, and M_r, represent the Mach number for the source.

Through the FFT, the SPL spectra can be obtained, and the noise measurement receiving points were placed in terms of the noise receiving point specified in the GB/T 2888–2008 (GB/T 2008). The monitoring points in the sound field were placed as illustrated in Fig. 8. A total of 12 measuring points were evenly set in a circular range with a radius of 1 m around the impeller. The measuring points at twelve positions with the chord of the airfoil at 0°, 30°, 60°, 90°, 120°, 150°, 180°, 210°, 240°, 270°, 300°, and 330° were chosen as the fixed observation points.

3. RESULTS AND DISCUSSION

3.1 Total Pressure Efficiency

To investigate aerodynamic performance directly, η was performed. η can be expressed with the Eq. (11) (Wu and Huang 2019).

$$\eta = \left(P_{Tout} - P_{Tin}\right)/P_w \tag{11}$$

where P_{Tout} and P_{Tin} denote the total pressure of outlet and inlet, respectively. η represents the total pressure efficiency and P_w denotes the shaft power. Figure 9 illustrates η of the impellers, which was simulated with a constant speed of 850 rpm under various operating conditions. It is evident that η increases gradually when Q decreases, whereas the growth rate of η gradually slows down with the Q diminishing. Under the operating conditions, the order of η is I-4 > I-3 > I-3 > I-1. It is obvious that the coupling bionic blade of I-4 shows the highest η among these impellers. Especially, under the designed operating conditions, η for I-4 reached 38.68% while it is 36.40% for I-1. η for the I-4 increased by 2.28%, which might result from the enhancement of the blade functional capacity after optimization (Yang *et al.* 2021).

3.2 Static Pressure on the Suction and Ps

To investigate the impact of the bionic structure on the static pressure, the cloud diagram was presented. The static pressure distribution on the pressure Ss of these four impellers was compared, as displayed in Fig. 10. It is observed that the pressure gradient close to the Bt varies dramatically. The value of the highest pressure on the pressure surface was presented in the direction

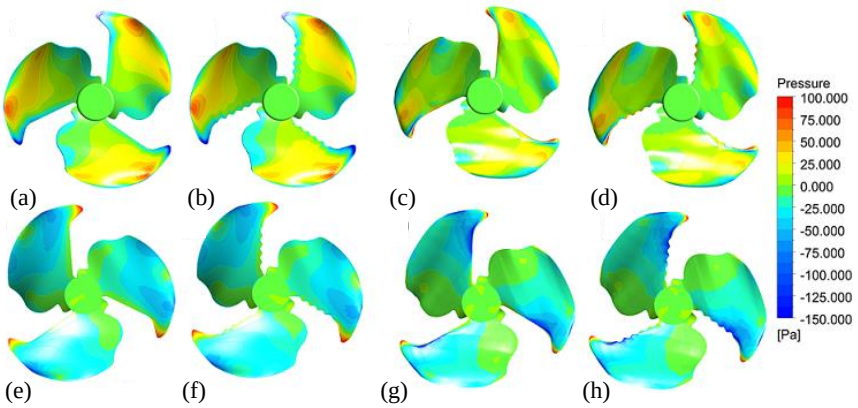

Fig. 10. Static pressure on the Ps and Ss: (a) the Ps of I-1, (b) I-2, (c) I-3, and (d) I-4; (e) the Ss of I-1, (f) I-2, (g) I-3, and (h) I-4.

of the Le chord line, which is 98 Pa for I-1, 90 Pa for I-2, 52 Pa for I-3, and 45 Pa for I-4. By optimizing the airfoil structure and Le, the fluctuation of pressure gradient on the surfaces becomes relatively uniform for the coupling bionic blade of I-4, compared to that for the other impellers, especially in the Te. Moreover, the pressure discrepancy in the Ss and Ps for I-4 is smaller than the other impellers, indicating the improved stress distribution for I-4. It might be due to the air flowing across the blade surface is more stable, resulting in a more uniform surface pressure distribution (Hua *et al.* 2019). The variation trend in the static pressure distribution conforms with the results obtained by Iwase (Iwase *et al.* 2017).

3.3 Static Pressure of Sections

To investigate the flow field on both sides of the impeller of an Aff directly, taking the original impeller model as an example, three sections are cut along the *Y*-axis of the impeller, which was located at Y = 10 mm, Y = –17 mm, and Y = –60 mm, respectively, and the position of each section is shown in Fig. 11.

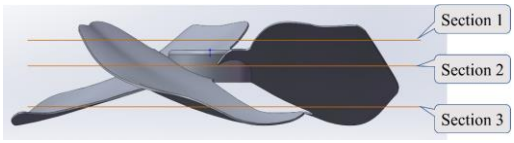

Fig. 11. The divided sections of the impellers.

As illustrated in Fig. 12, the blade static pressure exhibits a cyclically distribution along the direction of circumference, and rises progressively from the root to the tip along the radial direction. In addition, the Ss static pressure value in the negative pressure area for I-2, I-3, and I-4 gradually becomes smaller. Because of the Le structure, the distribution of the static pressure on suction surface for I-2, and I-4 becomes uniform gradually. Moreover, there is little distinction between the static pressure area for I-1 and I-2. Furthermore, the maximum static pressure (38 Pa) in section 1 of I-4 is apparently reduced compared with that of I-1 (12 Pa), and the static pressure area in section 2 and section 3 of I-4 is

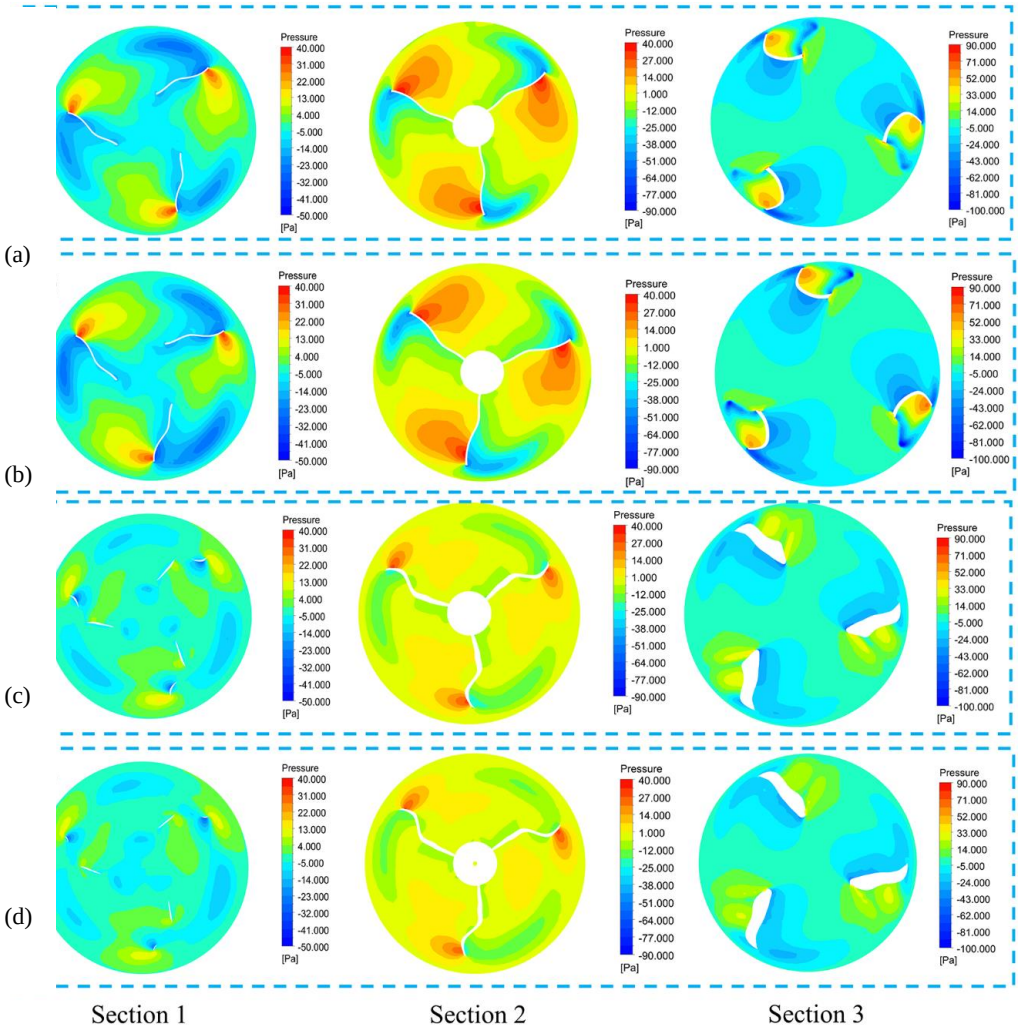

Fig. 12. Static pressure of sections: (a) I-1, (b) I-2, (c) I-3, and (d) I-4.

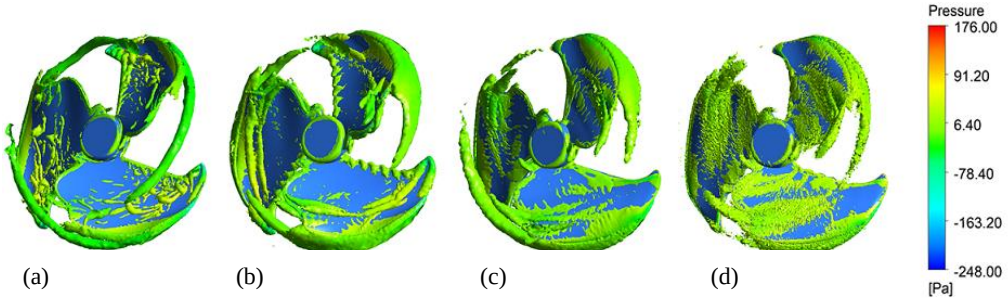

Fig. 13. Distribution of vorticity: (a) I-1, (b) I-2, (c) I-3, and (d) I-4.

greatly decreased relative to that of I-1.Additionally, the cross-section static pressure distribution of I-3 is similar to that of I-4, whereas the pressure distribution gradient of I-4 is more uniform than that of I-3. Besides, the high-pressure area for I-4 declines at the Bt and Le on the Ps, which is more uniform than that of I-1. Hence, there are the back-airflow and the cross-airflow on the Ps, causing the less disturbance flow, the lower thickness of turbulent boundary layer, and eventually the less flow loss (Yang *et al.* 2018). In consequence, the static pressure discrepancy in the Ss and Ps of the coupling bionic blade of I-4 lessens relative to that of I-1, and vortices and backflows from the Ps to the Ss of I-4 are hampered, resulting in a reduction in turbulence noise for I-4.

3.4 Distribution of Vorticity

To compare the evolution of airflow, the contours of vorticity on impellers, are displayed in Fig. 13. As we all know, the vorticity always result in broadband noise and large pressure fluctuations (Zhang *et al.* 2018). The large vortex structure in the direction of the vane span can be seen at the tail of I-1. In contrast, the eddy current structure area increases slightly to the Te for I-2 and I-3. Especially, due to the wavy Le and bionic airfoil for I-4, the eddy current structure area increases significantly to the Te, which gives rise to an increase in eddy current interaction and a remarkable decrease in flow separation around the Bt. Therefore, the convective vortex velocity and the broadband noise remarkably decrease for I-4. It might be due to the less separation bubble on the coupling bionic blade of I-4, which had positive influences on the performance and made the local surface pressure distribution more uniform, resulting in main flow steadiness (Mo and Choi 2020).

3.5 Axial Velocity of Airflow

The axial velocity can reflect the flow distribution and the flow separation. The axial velocity at the Le for these four impellers is relatively low, which results from the airfoil resistance (Xue *et al.* 2021), as illustrated in Fig. 14. The axial velocity raised progressively when the internal airflow traveled. With the strengthening of the blade's functional capacity, the corresponding mainstream axial velocity of each section increased. There is little difference between the axial velocity cloud images of section 1 and section 2 for I-4, whereas the high-speed area on the Ss of I-4 is oval, which is up to more than 12 m s^{-1} from the axial velocity cloud images of section 3 of I-4, demonstrating that the bionic blades can ensure Q of the outdoor unit. Since the influenced area expanded, the vortex cores traveled along the direction of radius, inducing the obstruction of the primary airflow and resulting in larger airflow loss (Luo *et al.* 2020), and similar regular axial velocity of the airflow was presented for I-1, I-2, and I-3.

3.6 Broadband Noise on Ps

This work analyzed the application of the seagull airfoil and the wavy Le blade for noise control. The noise emanating from the Ac outdoor unit is mainly composed of aerodynamic, broadband, and discrete noises. And the model of broadband noise was utilized to calculate the noise distributed on the impeller surface in this work. Thus, the steady value of acoustic power was calculated according to acoustic analogy. Figure 15 depicts the SPL on the impeller surface at 850 rpm, reflecting the pulsating pressure that the blade wall works on the flow, indicating the turbulent boundary layer's broadband noise level. The Ps is the working surface, resulting in the higher pressure pulsation and the larger SPL of broadband noise (Guo *et al.* 2022). Therefore, only the Ps average broadband noise was calculated in this work. Furthermore, the overall SPL for I-3 is relatively lower than that for I-1 by 3.59 dB, especially at the Bt, and the overall SPL for I-4 is close to that for I-3, while the overall SPL of the coupling bionic blade of I-4 decreases significantly at the Bt and the Le. Near the Le, considerable streamwise vorticity was generated and the pressure fluctuations decreased (particularly close to the hills of the Le) owing to the wavy structure, which hampered the unsteady forces (Tong *et al.* 2018).

3.7 Directivity of SPL

To investigate the interaction noise, A circle with a radius of 1 m was defined to calculate the

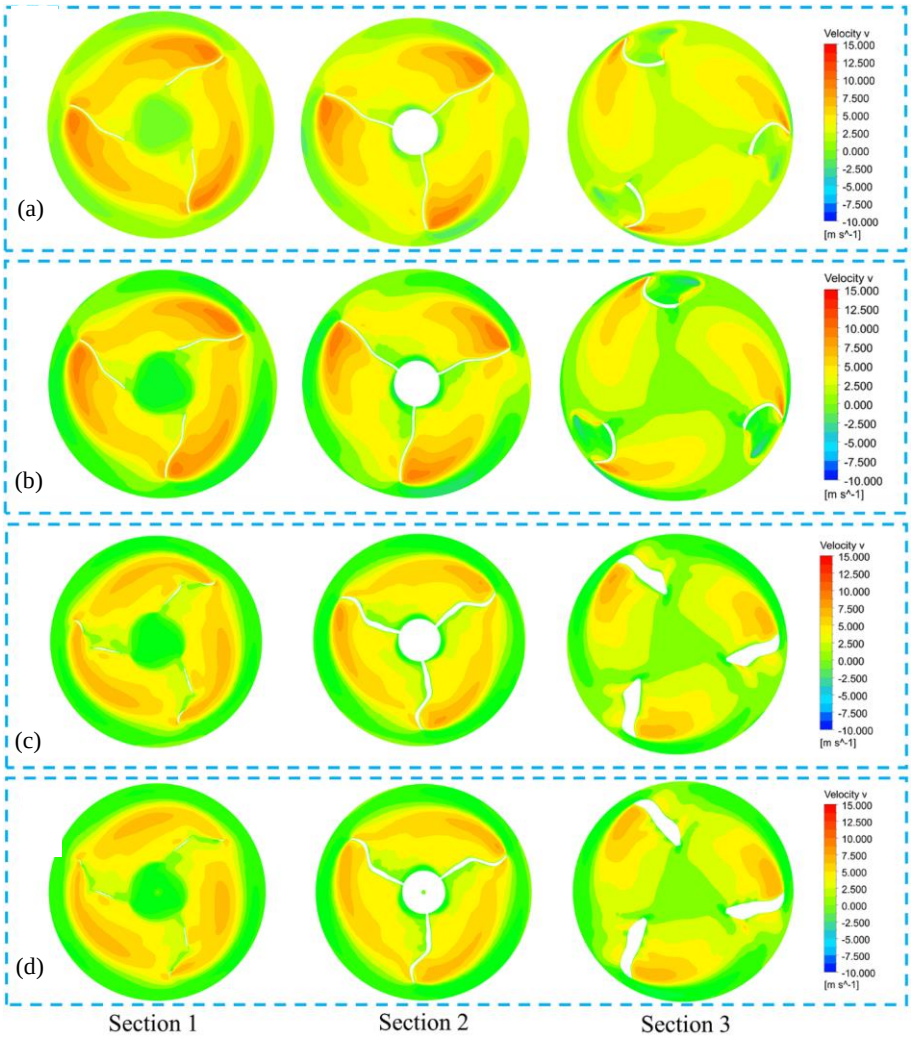

Fig. 14. Axial velocity of airflow: (a) I-1, (b) I-2, (c) I-3, and (d) I-4.

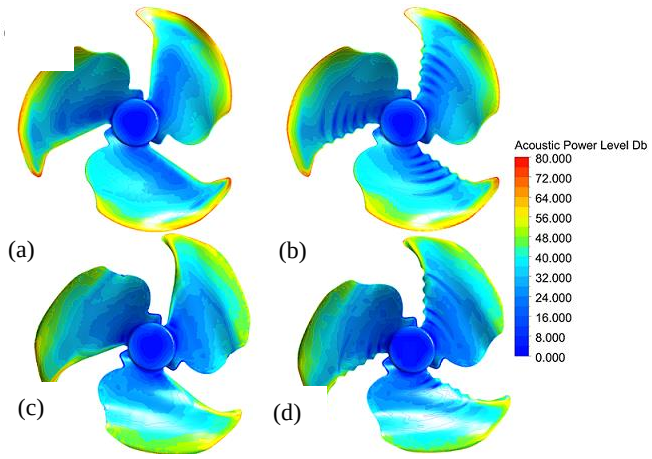

Fig. 15. Broadband noise on Ps: (a) I-1, (b) I-2, (c) I-3, and (d) I-4.

directivity of SPL. Fig. 16 illustrates comparison curves of the SPL at each monitoring point for these four impellers. Compared with I-1, I-2, and I-3, the coupling bionic blade of I-4 exhibits the lowest SPL for each monitoring point, which elucidates that the coupling bionic structure exhibits the more satisfying interaction noise reduction. According to

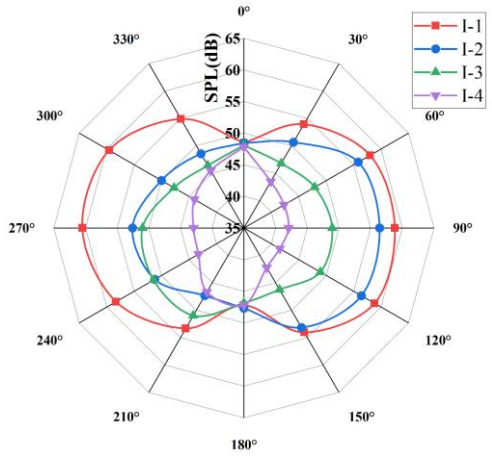

Fig. 16. Directivity of the SPL: (a) I-1, (b) I-2, (c) I-3, and (d) I-4.

the overall directivity distribution in I-1, I-2, and I-3, the SPL of the monitoring point at 90° and 270° is larger, mainly owing to the closer monitoring point to the whole blade. In contrast, the SPL at 90° and 270° for I-4 are relatively lower, demonstrating the excellent performance of the coupling bionic structure to reduce the SPL in the front direction. After optimization, the shape of SPL directivity gradually transformed from the '8' shape for I-1 to the '0' shape for I-4, exhibiting that the coupling bionic structure possessed a notable improvement in the SPL directivity, and the aerodynamic noise of the coupling bionic blade of I-4 decreased by 7.9 dB. Moreover, more attention should be paid to the acoustic performance of the location at 1 m in the front of the impeller in the air conditioning industry. Nevertheless, through the air intake grille, the front sound radiation significantly influences the acoustic performance (Peng *et al.* 2020). Taking the monitoring point at 90° as the reference point, it was found that the overall SPL at the monitoring point over 90° was higher than that at the monitoring point less than 90°. It mainly resulted from the speed changed of the blade on the front and back sides, inducing the postponement and promotion of the sound diffusion distance (Yu *et al.* 2020).

3.8 SPL Spectra

LES was used to perform an unsteady simulation in this work, and then, a Fourier transform was applied to carry out a spectrum analysis on the aeroacoustics noise derived from the Aff, as shown in Fig. 17. Compared with I-1, overall SPL distribution for I-2, I-3, and I-4 were improved in the Mf and Lf regions. The wavy Le of I-4 further reduced the broadband and discrete noise in the Mf and Lf range relative to I-3, especially, the noise reduction was more significantly around the region of 1000 Hz frequency. The coupling bionic blade further decreased the SPL around 3500 Hz in the condition of harmonics. Combined with the flow field analysis for these four impellers, the transition of suction to the Ps of I-4 is relatively smooth, which further improves the unsteady interaction between blade surfaces (Kroemer *et al.* 2018).

3.9 Modal Analysis

To estimate the security of the axial fan, the modal analysis of I-1 and I-4 are investigated and compared. First of all, the vibration modes of I-1 and I-4 under the free-free condition are presented in Fig. A1 and Fig. A2 (in the Appendix A), respectively. It is observed that the first, the second, and the third order of I-1 and I-4 display relatively minor bent deformation compared with the fourth to the eighth order. In addition, the fourth to the eighth order deformation of I-1 and I-4 appear to twist and the displacement gradually lessens from the outer diameter to the inner diameter, while the deformation of I-4 is distributed more uniformly. What's more, the vibration frequency of I-4 for each order was decreased compared with that of I-1, which indicates that the designed structure of I-4 was created reasonably. Moreover, the vibration modes of I-1 and I-4 under centrifugal load are displayed in Fig. A3 and Fig. A4, respectively. When the impellers rotate at the high speed, a large centrifugal load will be produced, causing an increment in the deformation and the vibration of I-1 and I-4 for each order. However, the vibration modes of I-1 and I-4 for each order under centrifugal load are similar to that under the free-free condition. Besides, the total deformation values and the vibration frequency of I-4 for each order are also lower than that of I-1, which suggests that I-4 would not resonate and break under centrifugal load. Furthermore, Fig. A5 and Fig. 18 display the vibration modes of I-1 and I-4 under centrifugal load and aerodynamic load, respectively. Table 2 listed the maximum total deformation of I-1 and I-4 for each order (from the first order to the eighth order). Fig. A5 and Fig. 18 presented that the vibration of I-1 and I-4 occurs only on the blades, and the maximum total deformation appears in the Bt, while the maximum total deformation of I-4 is smaller than that of I-1, especially in the seventh order. In addition, the first, the second, and the third order deformations of I-1 and I-4 are almost the same, and their deformation areas are concentrated. Besides, the fourth, the fifth, the sixth, the seventh, and the eighth order deformation of I-1 and I-4 distributed uniformly in the direction of circumference, and the effected region is expanded while the value of maximum total deformation decreased. The total deformation values and the vibration frequency of I-4 for each order are both smaller than that of I-1 in terms of the vibration of the blades and the maximum total deformation. Consequently, the modal analysis indicates the better vibration-damping effect of the designed coupling bionic blade (I-4) compared with I-1, which means the excellent security of I-4.

4. CONCLUSION

In this work, aerodynamic flow and noises (including aerodynamic, broadband, and discrete

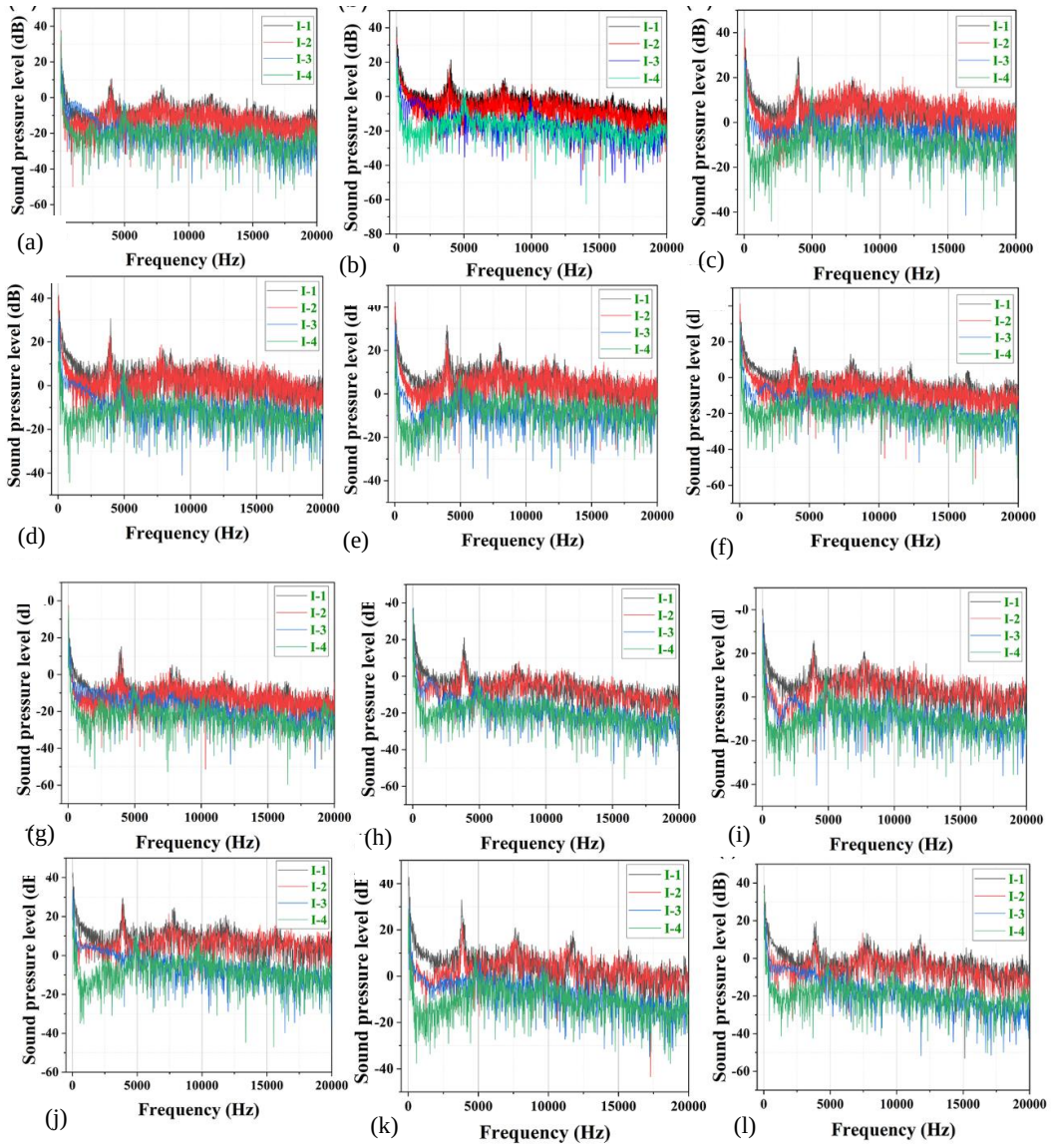

Fig. 17. SPL spectra at monitoring points: (a) 0°, (b) 30°, (c) 60°, (d) 90°, (e) 120°, (f) 150°, (g) 180°, (h) 210°, (i) 240°, (j) 270°, (k) 300°, and (l) 330°.

noises) radiated into the internal flow for four different impellers with the wavy Le and seagull airfoil have been numerically analyzed. SolidWorks software was used to construct the models, and Fluent software was used to carry out the numerical simulation process, which was conducted at the speed of 850 rpm. The results of the directivity of the SPL indicate that the impeller with the wavy Le and the seagull airfoil exhibit the outstanding capability to lessen the noise and enhance the aerodynamic performance. According to the results derived from this study, the coupling bionic blade of I-4 has a 2.28% η enhancement, a 3.59 dB broadband noise reduction, and a 7.9 dB aerodynamic noise reduction, indicating the coupling bionic blade could maintain aerodynamic performance for the air-conditioning system meanwhile reducing the noise. Furthermore, the modal analysis indicates the excellent security of I-4 compared with that of I-1. This study enriches the design methodologies applied in the Aff for further development. Derived from the present study, the conclusions can be list as following.

1. The blade functional capacity has been enhanced by the coupling bionic optimization, which significantly improved the aerodynamic property of the Aff.
2. Employing the coupling bionic optimization, the air flowing through the blade surface is more stable, leading to a more uniform surface pressure distribution. Hence, A lower static differential pressure is observed between the suction and pressure surfaces, and vortices and backflows from the Ps to the Ss are hampered, causing a reduction in turbulence noise.

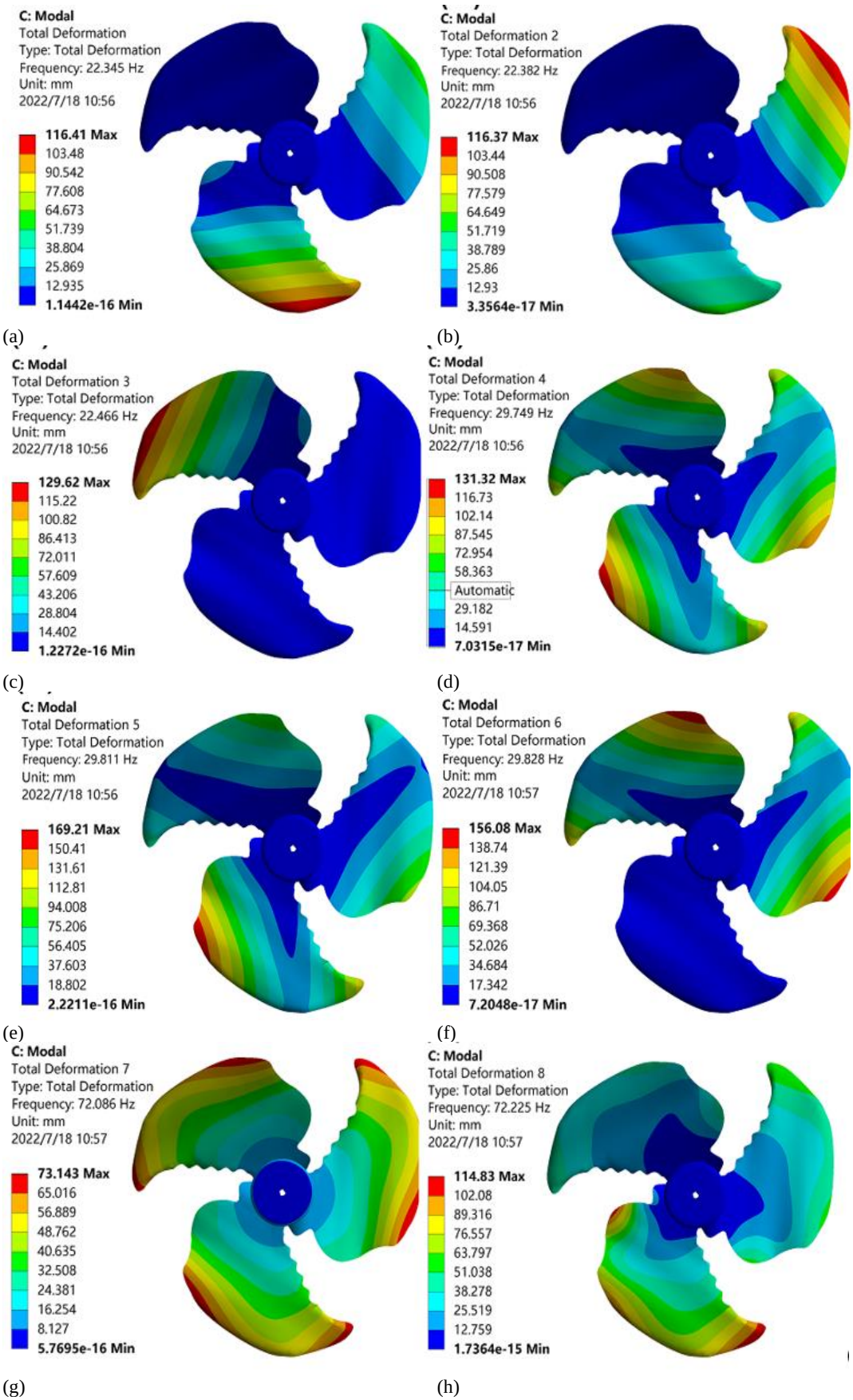

Fig. 18. Modal analysis from the first to the eighth order vibration modes (a–h) of I-4 under centrifugal load and aerodynamic load.

Table 2 Maximum total deformation of the first to the eighth order vibration modes of I-1 and I-4 (mm)

Order	I-1	I-4
1	374.19	116.41
2	374.16	116.37
3	374.47	129.62
4	247.77	131.32
5	188.03	169.21
6	193.61	156.08
7	412.62	73.143
8	413.46	114.83

3. The coupling bionic blade could transform the shape of directivity of SPL from the '8' shape to the '0' shape, and improve the SPL distribution in the Mf and Lf region significantly.

ACKNOWLEDGEMENTS

This work has been funded by the National Natural Science Foundation of China (Grant no. 21403184), the Qinglan Project of Jiangsu Province, the Natural Science Foundation of the Jiangsu Higher Education Institutions of China (Grant No. 22KJA430008), and the Scientific Research and Practical Innovation Project for Graduate Students in Jiangsu Province (No. SJCX21_XY015).

APPENDIX A. SUPPLEMENTARY MATERIAL

The modal analysis from the first to the eighth order vibration modes of I-1 under the free-free condition, I-4 under the free-free condition, I-1 under centrifugal load, I-4 under centrifugal load, and I-1 under centrifugal load and aerodynamic load.

REFERENCES

Abdolmaleki, M, H. Afshin and B. Farhanieh (2019). Performance analysis of elliptic-profile airfoil cascade for designing reversible axial flow fans. *Aiaa Journal* 57, 1492-1501.

Balla, E. and J. Vad (2019). Lift and drag force measurements on basic models of low-speed axial fan blade sections. *Proceedings of the Institution of Mechanical Engineers Part a-Journal of Power and Energy* 233, 165-175.

Bian, T., X. Shen, B. Wang, J. Feng and Q. Han (2019). Numerical and experimental investigation of flow loss and flow structure of circular arc cambered plate blade cascade. *Proceedings of the Institution of Mechanical Engineers Part a-Journal of Power and Energy* 233, 961-973.

Biedermann, T. M., F. Kameier and C. O. Paschereit (2019). Successive aeroacoustic transfer of leading edge serrations from single airfoil to low-pressure fan application. *Journal of Engineering for Gas Turbines and Power-Transactions of the Asme* 141, 453-465.

Brentner, K. S. (1988). Prediction of helicopter rotor discrete frequency noise for three scale models. *Journal of Aircraft* 25, 420-427.

Chaitanya, P., P. Joseph, S. Narayanan, C. Vanderwel, J. Turner, W. J. Kim and B. Ganapathisubramani (2017). Performance and mechanism of sinusoidal leading edge serrations for the reduction of turbulence–aerofoil interaction noise. *Journal of Fluid Mechanics* 818, 435-464.

Chang, X., L. Zhang, R. Ma and N. Wang (2019). Numerical investigation on aerodynamic performance of a bionic flapping wing. *Applied Mathematics and Mechanics-English Edition* 40, 1625-1646.

Chen, K., W. W. Yao, J. H. Wei, R. B. Gao and Y. X. Li (2021). Bionic coupling design and aerodynamic analysis of horizontal axis wind turbine blades. *Energy Science & Engineering* 9, 1826-1838.

Choi, J. S. (1994). Aerodynamic noise generation in centrifugal turbomachinery. *KSME Journal* 8, 161-173.

Corsini, A., G. Delibra and A. G. Sheard (2014). The application of sinusoidal blade-leading edges in a fan-design methodology to improve stall resistance. *Proceedings of the Institution of Mechanical Engineers Part a-Journal of Power and Energy* 228, 255-271.

Dong, X. and H. S. Dou (2021). Effects of bionic volute tongue bioinspired by leading edge of owl wing and its installation angle on performance of multi-blade centrifugal fan. *Journal of Applied Fluid Mechanics* 14, 1031-1043.

Farassat, F. and K. S. Brentner (1998). The acoustic analogy and the prediction of the noise of rotating blades. *Theoretical and Computational Fluid Dynamics* 10, 155-170.

Gao, R., K. Chen, Y. Li and W. Yao (2021). Investigation on aerodynamic performance of wind turbine blades coupled with airfoil and herringbone groove structure. *Journal of Renewable and Sustainable Energy* 13, 854-869.

GB/T, 1236-2017 (2017). Performance Test of Industrial Ventilator with Standardized Air Duct. China Standard Press.

GB/T, 2888-2008 (2008). Methods of Noise Measurement for Fans Blowers Compressors and Roots Blowers. China Standard Press.

Guo, R., T. Mi, L. Li and R. Luo (2022). Research on aerodynamic performance and noise reduction of high-voltage fans on fuel cell vehicles. *Applied Acoustics* 186, 108454.

Hua, X. (2013). *Research on the Aerodynamic Characteristics of Wings of the seagull and the blade design Application*. Ph. D. thesis, Jilin University, Jilin, China.

Hua, X., C. Zhang, J. Wei, X. Hu and H. Wei (2019). Wind turbine bionic blade design and performance analysis. *Journal of Visual Communication and Image Representation* 60, 258-265.

Iwase, T., T. Kishitani and M. Furukawa (2017). Study on influence of blade number on aerodynamic noise of half-ducted propeller fans for packaged air-conditioners. *International Journal of Fluid Machinery and Systems* 10, 318-327.

Jiang, B., J. Wang, X. Yang, W. Wang and Y. Ding (2019). Tonal noise reduction by unevenly spaced blades in a forward-curved-blades centrifugal fan. *Applied Acoustics* 146, 172-183.

Jung, J. H. and W. G. Joo (2019). The effect of the entrance hub geometry on the efficiency in an axial flow fan. *International Journal of Refrigeration* 101, 90-97.

Kim, J. W., S. Haeri, and P. F. Joseph (2016). On the reduction of aerofoil–turbulence interaction noise associated with wavy leading edges. *Journal of Fluid Mechanics* 792, 526-552.

Kroemer, F., A. Renz and S. Becker (2018a). Experimental investigation of the sound reduction by leading-edge serrations in axial fans. *Aiaa Journal* 56, 2086-2090.

Kroemer, F., F. Czwielong and S. Becker (2019). Experimental investigation of the sound emission of skewed axial fans with leading-edge serrations. *Aiaa Journal* 57, 5182-5196.

Kroemer, F. and S. Becker (2018b). Sound emission of low-pressure axial fans under distorted inflow conditions. *Journal of Aerospace Engineering*.

Lallier-Daniels, D., M. Piellard, B. Coutty, and S. Moreau (2017). Aeroacoustic study of an axial engine cooling module using lattice-Boltzmann simulations and the Ffowcs Williams and Hawkings' analogy. *European Journal of Mechanics B-Fluids* 61, 244-254.

Li, D., X. Liu, F. Hu and L. Wang (2020). Effect of trailing-edge serrations on noise reduction in a coupled bionic aerofoil inspired by barn owls. *Bioinspiration & Biomimetics* 15, 101901.

Li, D., X. Liu, L. Wang, F. Hu and G. Xi (2021). Numerical study on the airfoil self-noise of three owl-based wings with the trailing-edge serrations. *Proceedings of the Institution of Mechanical Engineers, Part G: Journal of Aerospace Engineering* 235, 2003-2016.

Li, Y., K. Chen, R. Gao, J. Wei and W. Yao (2022). Noise reduction of bionic coupling blades of horizontal axis wind turbine. *Noise Control Engineering Journal* 70, 169-187.

Lim, T. G., J. H. Jung, W. H. Jeon, W. G. Joo and G. Minorikawa (2020). Investigation study on the flow-induced noise by winglet and shroud shape of an axial flow fan at an outdoor unit of air conditioner. *Journal of Mechanical Science and Technology* 34, 2845-2853.

Liu, H., B. Liu, L. Li and H. Jiang (2003). Effect of leading-edge geometry on separation bubble on a NACA65 compressor blade. *Journal of Engineering Thermophysics* 24, 231-233.

Liu, H., Y. Lu, J. Yang, X. Wang, J. Ju, J. Tu, Z. Yang, H. Wang and X. Lai (2021b). Aeroacoustic optimization of the bionic leading edge of a typical blade for performance improvement. *Machines* 9.

Liu, H., Y. Lu, X. Wang, Y. Li, Y. Yan and X. Lai (2021a). Investigation of the effects of the vane blades on the CAP1400 nuclear coolant pump's performance based on a bionic strategy. *Nuclear Engineering and Design* 384, 379-394.

Luo, B., W. L. Chu and H. G. Zhang (2020). Tip leakage flow and aeroacoustics analysis of a low-speed axial fan. *Aerospace Science and Technology* 98, 105700.

Mo, J. O. and J. H. Choi (2020). Numerical investigation of unsteady flow and aerodynamic noise characteristics of an automotive axial cooling fan. *Applied Sciences-Basel* 10, 5432-5448.

Neise, W. (1992). Review of fan noise generation mechanisms and control methods. In *International Symposium on Fan Noise 1.-3.9.1992 Seulis, France*, Publications CETIM, Seulis, France.

Peng, Z., Y. Wu, J. Tian and H. Ouyang (2020). Discrete noise control of cooling fan module: Stator and rotor interaction. *Applied Acoustics* 165, 107308.

Sasaki, S., K. Suzuki, Y. Onomichi and H. Hayashi (2013). Influence of diffuser on aerodynamic noise of a forward curved fan. *Journal of Thermal Science* 22, 433-438.

Schram, C. and A. Hirschberg (2003). Application of vortex sound theory to vortex-pairing noise: sensitivity to errors in flow data. *Journal of Sound and Vibration* 266, 1079-1098.

Takahashi, T., K. Fukudome, H. Mamori, N. Fukushima and M. Yamamoto (2020). Effect of characteristic phenomena and temperature on super-cooled large droplet icing on NACA0012 Airfoil and axial fan blade. *Aerospace* 7, 7070092.

Tong, F., W. Qiao, K. Xu, L. Wang, W. Chen and X. Wang (2018). On the study of wavy leading-edge vanes to achieve low fan

interaction noise. *Journal of Sound and Vibration* 419, 200-226.

Tong, H., L. Li, L. Wang, L. Mao and W. Qiao (2021). Investigation of rotor-stator interaction broadband noise using a RANS-informed analytical method. *Chinese Journal of Aeronautics* 34, 53-66.

Wang, L., X. Liu and D. Li (2021). Noise reduction mechanism of airfoils with leading-edge serrations and surface ridges inspired by owl wings. *Physics of Fluids* 33, 015123.

Wang, L., X. Liu, L. Wu and D. Li (2022). Effect of the asymmetric bio-inspired trailing-edge serrations on sound suppression in a coupled owl-based airfoil. *Applied Acoustics* 191: 108667.

Wang, M. and X. Liu (2019). Numerical investigation of aerodynamic and acoustic characteristics of bionic airfoils inspired by bird wing. *Proceedings of the Institution of Mechanical Engineers, Part G: Journal of Aerospace Engineering* 233, 4004-4016.

Wen, X., D. Qi, Y. Mao and X. Yang (2013). Experimental and numerical study on the inlet nozzle of a small squirrel-cage fan. *Proceedings of the Institution of Mechanical Engineers, Part A: Journal of Power and Energy* 227, 450-463.

Wu, L. and X. Liu (2021). Dynamic stall characteristics of the bionic airfoil with different waviness ratios. *Applied Sciences-Basel* 11, 9943.

Wu, L., X. Liu, Y. Liu and G. Xi (2022). Using the combined flow control accessory to the aerodynamic performance enhancement of bio-inspired seagull airfoils. *Journal of Renewable and Sustainable Energy* 14, 534-548.

Wu, Y. J. and D. G. Huang (2019). Optimization design of axial fan blade. *Journal of the Chinese Institute of Engineers* 42, 473-478.

Xu, K., W. Qiao and L. Ji (2015). Experiment on noise reduction physical mechanism of serrated trailing edge structure. *Hangkong Dongli Xuebao/Journal of Aerospace Power* 30, 463-472.

Xue, L., J. Liu, D. Wang and L. Zhao (2021). Experimental and numerical simulation investigations of an axial flow fan performance in high-altitude environments. *Energy* 234: 121281.

Yan, H., C. Yu, L. Chai, Y. Li, V. Vnenkovskaia and H. Chen (2019). Design and investigation of the hydraulic performance of bionic hydrofoil based on the geometric features of sturgeons. *Dyna* 94, 278-285.

Yan, H., X. Su, H. Zhang, J. Hang, L. Zhou, Z. Liu and Z. Wang (2020). Design approach and hydrodynamic characteristics of a novel bionic airfoil. *Ocean Engineering* 216, 108076.

Yang, K., S. Q. Zhou, Y. J. Hu, H. X. Zhou and W. Y. Jin (2021). Energy efficiency optimization design of a forward-swept axial flow fan for heat pump. *Frontiers in Energy Research* 9, 700365.

Yang, X., C. Wu, H. Wen and L. Zhang (2018). Numerical simulation and experimental research on the aerodynamic performance of large marine axial flow fan with a perforated blade. *Journal of Low Frequency Noise, Vibration and Active Control* 37, 410-421.

Yu, P. X., J. H. Peng, J. Q. Bai, X. Han and X. Song (2020). Aeroacoustic and aerodynamic optimization of propeller blades. *Chinese Journal of Aeronautics* 33, 826-839.

Zhang, M., Y. Zhang, C. Cai, H. Cao and Z. Zhang (2021). A review on modeling of bionic flow control methods for large-scale wind turbine blades. *Journal of Thermal Science* 30, 743-757.

Zhang, W., J. Yuan, B. Zhou, H. Li and Y. Yuan (2018). The influence of axial-flow fan trailing edge structure on internal flow. *Advances in Mechanical Engineering*, 10: 1-12.

Zuo, S. G., C. F. Xie, X. D. Wu, Y. J. Li and K. J. Wei (2019). Numerical simulation and optimization of aerodynamic noise for claw pole alternator. *Proceedings of the Institution of Mechanical Engineers* 233, 857-879.